Investigation of the Electrode Materials in Conductive Bridging RAM from First-Principle

F. Ducry, K. Portner, S. Andermatt, M. Luisier
Integrated Systems Laboratory
ETH Zurich
CH-8092 Zurich, Switzerland
E-mail: fabian.ducry@iis.ee.ethz.ch

***Abstract*—Conductive bridging random access memories (CBRAM) are emerging non-volatile data storage devices whose switching mechanisms are not fully understood. Here, we present a modelling framework based on *ab-initio* simulations to investigate CBRAM cells. It combines density-functional theory and the Non-equilibrium Greens Function formalism. Realistic metallic filaments connecting two electrodes are constructed and their ballistic transport characteristics studied. For a given filament the type of counter electrode material has little influence on the magnitude of the ON-state current, but affects its spatial distribution. The conductance mainly depends on the material of the active electrode and the shape of the thinnest part of the filament.**

I. Introduction

Conductive bridging random access memories (CBRAM) are promising candidates as non-volatile data storage units due to their low energy consumption, fast switching speed, large ON-OFF ratio, and outstanding scalability [1]. This technology relies on the reversible growth of a metallic filament through an insulator from an inert counter electrode (CE) towards an active electrode (AE), as illustrated in Fig. 1a. The data is encoded through different resistance states realized by growing or dissolving the filament. The latter is stable, even without an applied electric field, and therefore able to retain its state for long time periods. Many material combinations have been reported to support filament growth [2]. Hence, a large parameter space is available to optimize the performance of CBRAM.

Device simulations represent a convenient way to investigate the properties of different CBRAM configurations and compare their performance. However, due to the small dimensionality of these devices, interface interactions and the atomic granularity of the filament play a crucial role. They are usually difficult to capture by computer aided design [3]. Thus, the models need to be carefully parametrized [4]. *Ab-initio* simulation approaches circumvent these restrictions, but are usually limited to a few 100 atoms. This is problematic as allowing for lattice mismatches between the different crystalline materials of the AE and CE requires large system sizes or the application of strain [5]. Here, an *ab-initio* quantum transport solver capable of treating systems composed of several thousand atoms is used to study how the choice of the AE and CE materials influences the behavior of ultra-scaled CBRAM cells.

II. Approach

Two CBRAM configurations are investigated, one with Ag, the other with Cu as AE material. They are combined with Pt and W as CE. For Ag and Cu, the $<111>$-crystal surface is used at the metal-insulator interface. The Pt and W crystals are rotated as necessary to achieve strain below 1% in each material, which is equally shared between the AE and CE. As insulator, we use amorphous SiO_2 (a-SiO_2). The resulting layer separates the electrodes. Due to its amorphous nature, it adapts to any cross-section dimension without inducing strain. The a-SiO_2 has a thickness of 2 nm and the metal contacts measure between 3.4 nm and 6.8 nm in length with a cross-sections of 2.4x2.5 nm^2 or 2.8x2.3 nm^2, resulting in structures with up to 5453 atoms.

Multiple steps of *ab-initio* molecular dynamics (AIMD) and geometry optimization within density functional theory (DFT) [6], [7] are needed to construct the modeled structures, as shown in Fig. 1b. Prior to the DFT stage, the a-SiO_2 is obtained by a melt-and-quench approach using force-field molecular dynamics (FFMD), as detailed in Fig. 1c. A SiO_2 β-cristobalite crystal is melted at 5000 K for 550 ps. To speed up the melting process the volume is increased by a factor of 2.75 during the first 300 ps. Subsequently, the sample is re-scaled to the target density and annealed for another 250 ps. Then, the SiO_2 is cooled down to room temperature at 40 K/ps and constant volume and lastly further annealed for 40 ps at 300 K. To start the DFT process, AE contacts are attached on two sides of the a-SiO_2 and the latter optimized. During this process the contact atoms remain immobile. In order to reduce the computational cost, the same material is used for both contacts, eliminating the AE-CE metal interface periodic boundary conditions (PBC) would lead to. Next, the filament is inserted by either replacing all Si and O atoms by Ag or Cu atoms within a cone or by removing all Si and O atoms within a cone and inserting a cone of crystalline AE metal. The system is again relaxed using optimization and AIMD for 1.5 ps, now including the top three electrode atom layers. After annealing, the filament is no longer perfectly conical, but assumes a shape that minimizes its potential energy, as illustrated in Fig. 2. Finally, the bottom contact is replaced by an inert metal (Pt or W). To preserve the filament-AE interface, only the filaments basis near the CE and the top CE layers are

978-1-5386-6790-3/18/$31.00 ©2018 IEEE

annealed for 0.5 ps.

Devices in the OFF-state are created in two different manners. The first approach is similar to the above described procedure, except that no filament is inserted, thus creating simple metal-insulator-metal devices. This requires longer annealing times of over 5 ps in total. Otherwise the quality of the oxide is low so that current can flow along defects. Alternatively, the OFF-state can be obtained by manipulating the Hamiltonian matrix resulting from the ON-state devices. By removing all rows and columns corresponding to filament atoms, one can create an insulating structure with similar conductances as the ones created through the first method.

The FFMD simulations are performed with an empirical pairwise potential [8], as implemented in the Atomistix Tool Kit [9], while the DFT calculations are done in CP2K [10] with GTH pseudopotentials [11] and the PBE exchange-correlation functional [12]. For metals, DZVP basis sets [13] are employed, 3SP [14] for Si and O. To compute the Hamiltonian, the metal atoms are expressed in SZV basis sets instead of DZVP, as they provide accurate results at much lower computational cost [15]. Owing to the large cell size only Γ-point sampling was used.

Based on the Hamiltonian and overlap matrices obtained from DFT, electron transport simulations are carried out via a quantum mechanical device solver relying on the Non-equilibrium Green's Function (NEGF) formalism [16]. Due to the localized nature of the Gaussian basis functions, the Hamiltonian has a sparse and banded form, as illustrated in Fig. 3a: it resembles a tight-binding Hamiltonian. As PBC are used throughout the DFT calculations, special care is required to treat the boundaries due to the AE-CE metal-metal interface across the cell boundary. The non-zero entries in the Hamiltonian corresponding to the PBC are removed. As the metal-metal interface also affects the diagonal elements of the Hamiltonian close to the interface, the entries corresponding to the first few layers of metal atoms from the most left and rightest parts of the CBRAM cell are deleted, shrinking the size of the Hamiltonian. The extent of the interface is determined from the PBC blocks and typically is up to six layers in calculations using the SZV basis set. After the cut, both ends of the Hamiltonian correspond to bulk AE and CE materials, respectively. The overlap matrix is treated analogously.

III. Results

The structure of the filament after annealing is mostly crystalline if the diameter is larger than 7 Å. Thinner parts and the surface remain amorphous and the local atomic arrangement strongly depends on the surrounding oxide configuration. This feature is independent of the method of insertion. Filaments created by atom replacement will crystallize, whereas crystalline inserted filaments will grow amorphous at the tip and surface, as can be seen in Fig. 2.

The ballistic transmission function of the created devices has been first computed. The results are displayed in Fig. 3b for cells with an Ag filament and three different CE metals. All plotted curves exhibit peaks of equal magnitude at the same energies. The very similar shape directly translates into almost identical low-field I-V characteristics, as reported in Fig. 3c. The conductance of the CBRAM cell can be extracted from a linear fit of the I-V's and is given for all devices with and without a filament in Fig. 4a. The filament conductances are 0.17 G_0 and 0.64 G_0 for Ag and Cu, respectively. Both values are well within the range of experimental ON-state conductances. The value of the ON-state conductance stays in a very narrow range for all structures with the same AE, demonstrating that the CE metal has little influence on the transmission probability. The conductance appears to be rather determined by the filament-AE interface and the filament geometry. As a consequence, the difference between the Ag and Cu cells can be attributed both to the different shape of the filaments and the different AE metals.

The OFF-state conductances are all close to each other and more than four orders of magnitude lower than their ON-state counterparts. This indicates that the OFF-state is primarily determined by the a-SiO_2 layer and independent of the electrode metals. The very low OFF-state conductance is in part due to the small cross-section of the model of 5.9 nm^2. However, increasing the cross-section to an area of 10 mn x 10 nm increases the area by a factor of 17 and decreases the resistance by the same factor. This still yields an ON-OFF ratio of more than 3 orders of magnitude, which suggests that 2 nm of a-SiO_2 suffice to switch a cell OFF for ultra-scaled CBRAM.

Both methods to compute the OFF-state transmission function produce similar results, as demonstrated in Fig. 4b. While the manipulated Hamiltonian gives slightly different shapes, the overall agreement is striking. The removal of atoms from the Hamiltonian therefore constitutes a computationally cheap method to estimate the OFF-state conductance.

While an important device characteristic, the cell conductance gives little insight into the flow of the current. To determine its spatial distribution, the current density throughout the devices has been computed and is depicted with contour plots in Fig. 5a. It is apparent that the current distribution through the tip and AE is independent of the CE, while the filament-CE interface is affected. As the current magnitude is equal, this shows that the conductance is determined by the filament tip and filament-AE interface. A visualization of the current trajectories is shown in Fig. 5b.

IV. Conclusion

We have studied the electrical properties of realistically sized CBRAM cells at the *ab-initio* level. By comparing different contact materials, the influence of the electrode type on the ON- and OFF-state has been investigated. The counter electrode material is found to exert little influence on the current magnitude, but more on its trajectories. Consequently, models using identical material for both electrodes can accurately capture the I-V characteristics of CBRAM cells with a predefined filament.

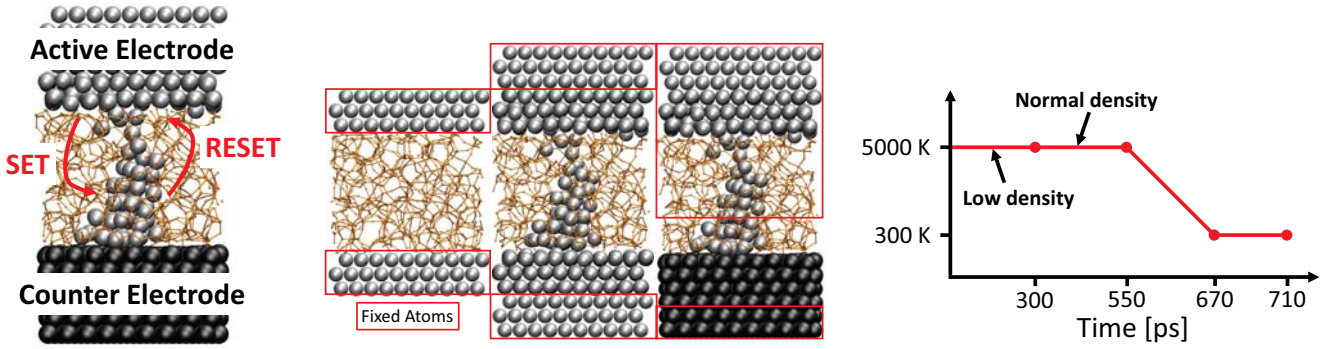

(a) Operating Principle (b) Model Assembly Stages (c) Melt and Quench

Fig. 1. (a) Atomistic CBRAM model illustrating the operating principle of the device. The top contact is the active electrode (AE) made of Ag or Cu, the bottom contact the counter electrode (CE) made of W or Pt. The a-SiO_2 matrix is represented by its bonds only. A metallic filament of the same material as the AE bridges the gap. The arrows indicate the cation movement during the switching processes, down for the SET and upwards for the RESET process. (b) Assembly steps of the CBRAM cell. A metal, Ag or Cu, contact is attached to the produced a-SiO_2 and the latter optimized with DFT. Next, the filament is inserted and the contacts extended. The filament and the top metal layers are relaxed and annealed with AIMD. Finally, the CE is replaced with an electro-chemically inert metal, Pt or W. The CE surface and the bottom of the filament are further annealed. (c) Time line of the melt-and-quench procedure using FFMD. The SiO_2 is melted at 5000 K, cooled down to room temperature at 40 K/ps and further annealed at 300 K.

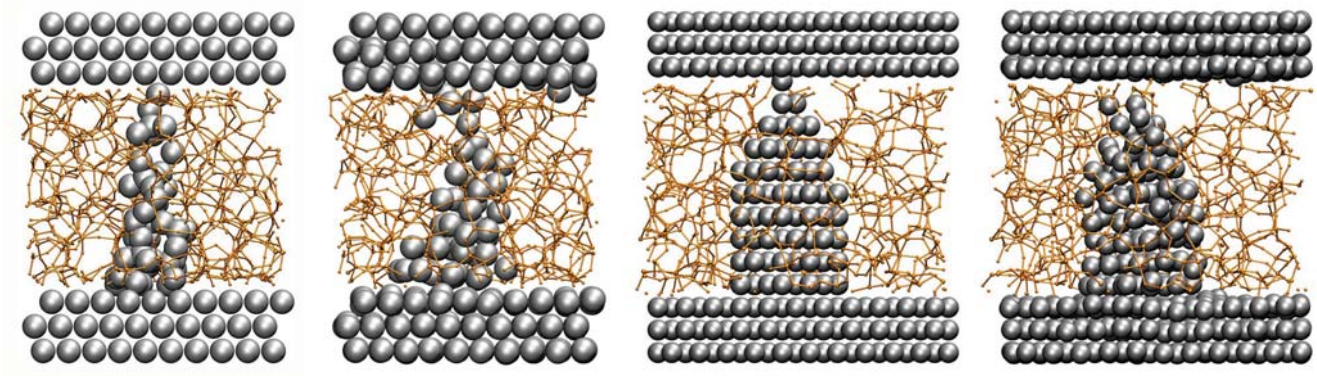

(a) Ag filament as inserted (b) Ag filament annealed (c) Cu filament as inserted (d) Cu filament annealed

Fig. 2. Schematic view of the filaments considered in this work before and after annealing. Both contacts are made of Ag or Cu, as is the filament. Only the metal atoms are shown, while the a-SiO_2 represented by its bonds. (a) Ag filament as inserted by converting all Si and O atoms to Ag. (b) Same filament as in (a) after the annealing procedure. The lowest two layers of atoms crystallize, above the wire is too narrow for this process and the filament remains amorphous. (c) Crystalline Cu filament inserted into the a-SiO_2 matrix. (d) Same as (c), but after annealing. The sharp tip is lost and the surface grows distorted. The crystalline nature, however, is mostly retained through much of the nano-filament.

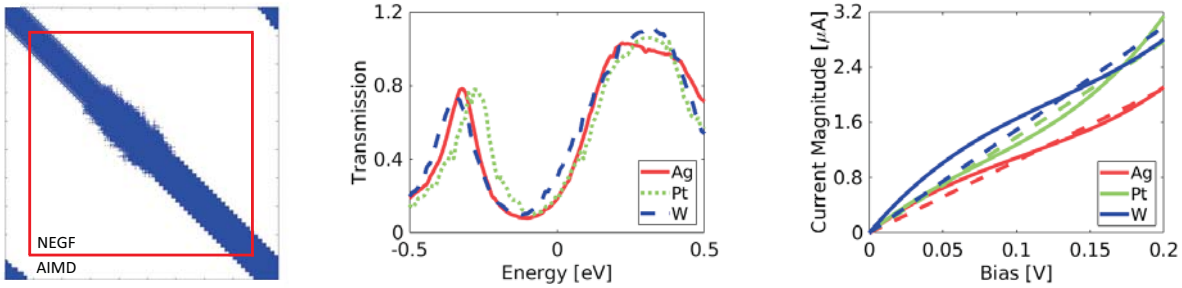

(a) Hamiltonian of the Pt-Ag model (b) Transmission with an Ag Filament (c) IV with an Ag Filament

Fig. 3. (a) Visualization of the calculations, Hamiltonian computed by CP2K. The matrix is banded except for entries in the top right and bottom left which are caused by the PBC. For the NEGF the columns and rows outside the central frame are discarded and only the framed part is retained. (b) Transmission function in the CBRAM ON-state for three different CE materials (Ag, Pt, W) in case of an Ag AE. The Fermi energy is set to 0 eV. The curves show the same peaks of equal height at -0.32 eV and 0.3 eV. (c) I-V characteristics of the same devices as in (b). The dashed lines represent linear fits of the IV-curves. The conductance values extracted from the fits are close to each other, ranging from 0.13 G_0 to 0.18 G_0.

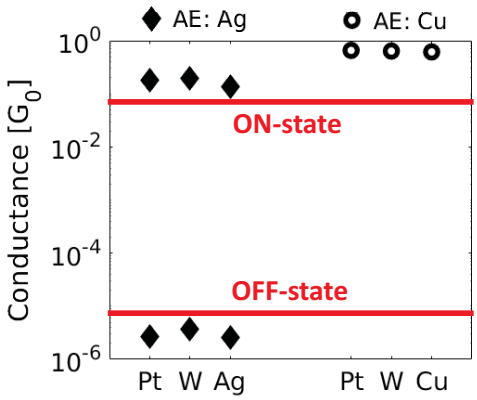

(a) Conductance of all devices

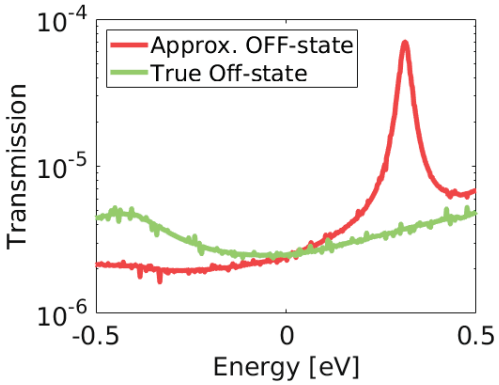

(b) Transmission in the OFF-state of the Ag-SiO_2-Ag model

Fig. 4. (a) Conductance value of all simulated devices with (ON-state) and without (OFF-state) the presence of a metallic filament in the a-SiO_2. (b) Transmission function in the OFF-state with Ag in the AE and CE. The values are of the same order of magnitude even though the shape of the functions does not perfectly agree.

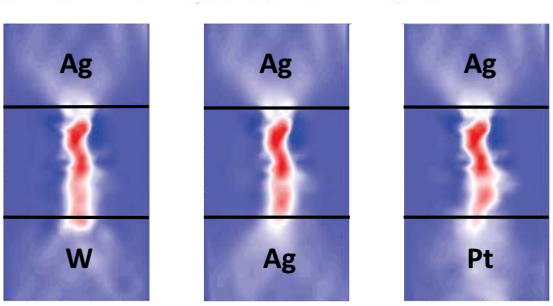

(a) Current density contour

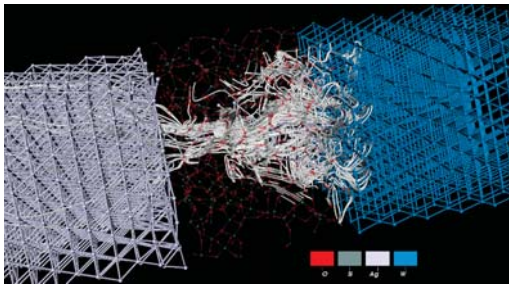

(b) Current field lines

Fig. 5. (a) Current density plots extracted in a slice taken through the Ag filament with three different CE metals, W, Ag, and Pt. The current densities in the AE and tip of the filament are identical, but differ in the CE and filament basis. (b) 3D visualization of the current passing through the filament. The white lines follow the current vector field.

Acknowledgement

This work was supported by the Werner Siemens Stiftung, by SNF under Grant No. PP00P2 159314, by ETH Research Grant ETH-35 15-2, and by a grant from the Swiss National Supercomputing Centre (CSCS) under project ID s714.

References

[1] C. Wang et al., *Microelectronic Engineering*, vol. 187-188, pp. 121–133, 2018.

[2] S. Menzel, *Journal of Computational Electronics*, vol. 16, pp. 1017–1037, 2017.

[3] I. Valov, *Semicond. Sci. Technol*, vol. 32, pp. 093006–093026, 2017.

[4] D. Ielmini, *Semiconductor Science and Technology*, vol. 31, pp. 063002–063027, 2016.

[5] H. Nakamura et al., *Phys. Chem. Chem. Phys.*, vol. 18, pp. 8820–8826, 2016.

[6] P. Hohenberg et al., *Physical Review*, vol. 136, pp. B864, 1964.

[7] W. Kohn et al., *Physical Review*, vol. 140, pp. A1133–A1138, 1965.

[8] A. Pedone et al., *Journal of Physical Chemistry B*, vol. 110, pp. 11 780–11 795, 2006.

[9] "Atomistix ToolKit version 2017.0, QuantumWise A/S (www.quantumwise.com)."

[10] J. VandeVondele et al., *Computer Physics Communications*, vol. 167, pp. 103–128, 2005.

[11] S. Goedecker et al., *Physical Review B*, vol. 54, p. 1703, 1996.

[12] J. Perdew et al., *Physical Review Letters*, vol. 77, pp. 3865–3868, 1996.

[13] J. VandeVondele et al., *The Journal of Chemical Physics*, vol. 127, p. 114105, 2007.

[14] E. S. Zijlstra et al., *Modelling and Simulation in Materials Science and Engineering*, vol. 17, pp. 015009–015019, 2009.

[15] F. Ducry et al., in *2017 IEEE International Electron Devices Meeting (IEDM)*, pp. 4.2.1–4.2.4, 2017.

[16] M. Luisier et al., *Physical Review B - Condensed Matter and Materials Physics*, vol. 74, pp. 205323–205335, 2006.